Modeled subglacial water flow routing supports localized intrusive heating as a possible cause of basal melting of Mars' south polar ice cap

N. S. Arnold[1], S. J. Conway[2], F. E. G. Butcher[3] and M. R. Balme[3]

[1]A Scott Polar Research Institute, University of Cambridge, Lensfield Road, Cambridge CB2 1ER, UK.

[2] CNRS, Laboratoire de Planétologie et Géodynamique, UMR 6112, 2, rue de la Houssinière BP 92208, France.

[3] School of Physical Sciences, The Open University, Walton Hall, Milton Keynes MK7 6AA, UK.

Corresponding author: Neil Arnold (nsa12@cam.ac.uk)

Key Points:

- We calculate the subglacial hydraulic potential for the Martian south polar ice cap from measured surface topography and ice thickness.
- The recently-observed area of inferred basal melt does not occupy a predicted depression in the subglacial hydraulic potential surface.
- We argue this supports the hypothesis that local geothermal heating could be responsible for this area of liquid.

Abstract

The discovery of a ~20 km wide area of bright subsurface radar reflections, interpreted as liquid water, beneath the Martian south polar layered deposits (SPLD) in data from the Mars Advanced Radar for Subsurface and Ionosphere Sounding (MARSIS) instrument, and the discovery of two geologically recent potential eskers (landforms produced by subglacial melt) associated with viscous flow features in Martian mid-latitudes, has suggested recent basal melting of Martian ice deposits may be feasible, possibly due to locally elevated geothermal heating. Locations of terrestrial subglacial lakes and major drainage axes have been successfully predicted from subglacial hydraulic potential surfaces calculated from surface topography and ice thickness. Here, we use surface topography from the Mars Orbiter Laser Altimeter and SPLD bed elevations derived from MARSIS data to calculate the subglacial hydraulic potential surface beneath the SPLD and determine whether the observed high reflectance area coincides with predicted subglacial lake locations. Given the sensitivity of terrestrial predictions of lake locations to basal topography, we derive over 1000 perturbed topographies (using noise statistics from the MARSIS data) to infer the most likely locations of possible subglacial water bodies and drainage axes. Our results show that the high reflectance area does not coincide with any substantial predicted lake locations; three nearby lake locations are robustly predicted however. We interpret this result as suggesting that the high reflectance area (assuming the interpretation as liquid is correct) is most likely a hydraulically-isolated patch of liquid confined by the surrounding cold-based ice, rather than a topographically-constrained subglacial lake.

Plain Language Summary

Mars' present-day ice deposits are generally assumed to be frozen throughout given its cold climate. However, new evidence from orbital radar data suggests a possible present-day ~20 km wide area of liquid water beneath Mars' south polar ice cap. Recently-discovered landforms in Mars' mid-latitudes have been interpreted as eskers (landforms produced by flowing meltwater beneath glaciers on Earth) and also suggest that subglacial melt may be feasible in Mars' recent past. Subglacial lakes are common on Earth, and their locations have been successfully predicted from ice surface topography and ice thickness, in conjunction with theories for subglacial water flow. In this paper we use the surface topography and ice thickness data for Mars' south polar ice cap to calculate the theoretical locations of possible subglacial lakes, and compare these with the location of the possible present-day area of liquid water. The observed patch of possible liquid water does not coincide with the lake locations we predict. We interpret this result as implying that the liquid water is most likely to be an isolated patch of liquid, possibly caused by locally-raised geothermal heating, and which is fixed in position by the surrounding frozen ice, rather than the liquid forming a topographically-constrained subglacial lake.

1 Introduction

Ice sheets, glaciers and ground ice distributed between Mars' poles and mid-latitudes [e.g. *Plaut et al.,* 2007; *Levy et al.,* 2014; *Souness and Hubbard,* 2012; *Head et al.,* 2003] contain a total volume of water ice (estimated as ~3.5 x 10^6 km^3), comparable to that of all glaciers on Earth excluding the East Antarctic Ice Sheet [*Levy et al.,* 2014], Mars' existing ice deposits are thought to have formed ~100s to Myrs ago [e.g. *Head et al.,* 2003; *Arfstrom and Hartmann,* 2005; *Butcher et al.,* 2017; *Conway et al.,* 2018], with landforms and models also indicating episodic glaciation of different regions of Mars' surface over billions of years [e.g. *Fastook et al.,* 2008; *Wordsworth et al.,* 2013; *Butcher et al.,* 2016]. Glaciers and ice sheets insulate a planet's surface, trapping geothermal heat from the planetary interior and frictional heat produced by ice flow, typically making their beds warmer than their surfaces. However, it is commonly thought that Mars' climate has been cold and dry for ~2–3 Gyr, and hence that the existing glaciers and ice caps have most probably been frozen throughout [e.g. *Levy et al.,* 2016], although there is some evidence for spatially-limited, ephemeral supraglacial melt [e.g. *Fassett et al.,* 2010]. The migration of ice between different reservoirs at different locations on Mars over this period is thought to have taken place via sublimation and (solid) precipitation, rather than melt [*Bramson et al.* 2017].

In contrast, recent geomorphological studies found evidence for localized melting beneath two existing mid-latitude glaciers around 110–150 Myr ago (Ma), in the form of subglacially-deposited eskers in Phlegra Montes and Tempe Terra [*Gallagher and Balme,* 2015, *Butcher et al.,* 2017]. Furthermore, that present day glaciers and ice caps are frozen throughout has also been challenged by the discovery of possible present-day liquid water beneath Mars' South Polar Layered Deposits [SPLD; *Orosei et al.,* 2018], based on anomalously bright subsurface reflections recorded by the MARSIS (Mars Advanced Radar for Subsurface and Ionospheric Sounding) instrument in a well-defined, 20 kilometer wide zone centered at 193°E, 81°S. In all three locations, elevated geothermal heating (e.g. due to localized magmatic intrusions) has been proposed as a possible source of the heat needed to melt the basal ice under cold current and recent Martian climate conditions [*Sori and Bramson,* 2019, *Butcher et al.,* 2017, *Gallagher and Balme,* 2015]. In addition, perchlorate salts, which substantially lower the melting point of ice to around ~200 to 230K depending on the concentration and species of perchlorate, may be highly enriched in the basal layers of the Martian polar ice caps [*Fisher et al.,* 2010; *Sori and Bramson,* 2019].

Subglacial water is far more common on Earth, occurring beneath the bulk of terrestrial valley glaciers, and both the Greenland and Antarctic Ice Sheets. In the case of Antarctica, large numbers of subglacial lakes, including Lake Vostok, the 6th largest (by volume) lake on Earth, have been detected by observing bright reflectances from numerous ground penetrating radar systems. Movement of water between subglacial lakes in large episodic drainage events has also been observed using localized changes in surface topography as lakes drain and fill. There is also a great deal of evidence for widespread subglacial meltwater in the landscapes occupied by ice during the Quaternary (and earlier) glaciations on Earth [e.g. *Shreve,* 1985*; Storrar et al.,* 2013, *Stroeven et al.,* 2016; *Clark et al.,* 2017].

The physics of subglacial water flow are well known. *Flowers* [2015] provides a comprehensive review, but briefly, the overall pattern of subglacial water flow is governed by the subglacial potential surface (calculated from the subglacial topography and ice thickness distribution; *Shreve,* [1972]). Local depressions in the potential surface form the nuclei for

possible subglacial lakes, as water cannot escape from such depressions until it fills to the elevation of the local 'spill point', the elevation of the lowest point in the constraining potential surface. Calculations of subglacial potential using digital elevation models (DEMs) of ice surfaces and ice thickness (or bed elevations) have proved very successful at predicting subglacial lake locations and volumes for terrestrial ice sheets. In a study of Antarctic lake locations, *Willis et al.,* [2016] show that the centers of lake locations predicted using the calculated subglacial potential surface were a mean distance of 6.3 km from the centers of the 379 known (in 2016) lakes. *Willis et al.,* [2016] predict around 100 times as many possible lake locations as the number of known lakes however. Some of this mis-match will be due to the size and remoteness of Antarctica, meaning that the current lake inventory will be incomplete. However, some of the mis-match will be due to errors of commission, where the potential surface predicts a lake where no lake exists. Such errors may be caused by inaccuracies in the surface or bed DEMs due to inaccuracies and/or resolution effects in the sensors, or the interpolation of relatively sparse point data onto a regular grid.

Several studies have shown that quite small changes in the bed and particularly the surface elevation can cause substantial changes in predicted subglacial water flow directions and lake locations. *Wright et al.,* [2008] found that raising three grid cells in the surface DEM by 10 m led to water flow switching between two major outlets from East Antarctica, and subsequently lowering another four surface DEM cells by 10 m led to another switch between two other large outlet glaciers. *Le Brocq et al.,* [2009] report similar sensitivity to small (~10 m) changes in surface elevation that divert flow between two major ice streams draining the Siple Coast of West Antarctica.

Uncertainties in data will also affect the predicted location of subglacial lakes. *Livingstone et al.,* [2013a] used current bed topography and modeled ice thickness distributions and isostatic effects from a suite of ice-dynamic reconstructions of the geometry of the North American Ice Sheets during the last glaciation on Earth to predict possible subglacial palaeo-lake locations. They found that lake locations (and inferred water flow directions) were highly sensitive to the configuration of the ice sheet at particular stages during ice sheet growth and decay, and depended in some instances on the choice of model and the predicted ice thickness distribution. They found that some predicted lakes were persistent through time, and were also predicted by many of the modeled ice sheet configurations, whereas other predicted lakes were present in fewer simulations, or were more transient features through time. Overall, deeper predicted lakes in areas of more pronounced topography (e.g. beneath the Cordilleran Ice Sheet in western North America) were more persistent. In another study, *Livingstone et al.,* [2013b] investigated the impact of errors or uncertainty in the basal topography of Antarctica on predicted subglacial lake locations by perturbing the bed topography using random noise with a standard deviation equal to the uncertainty in the bed elevation. They performed 50 such perturbations to produce a 'persistence map' of lakes, in which the most persistent lakes were those which were predicted in the majority of the perturbed-bed experiments.

In this paper we use gridded surface and ice thickness maps for the Martian South Polar Layered Deposit [SPLD; *Plaut et al.,* 2007] to calculate the subglacial hydraulic potential. From this, we infer the locations of depressions in the potential surface that would be expected to confine possible subglacial water bodies were basal meltwater available beneath the SPLD. We also predict the main drainage axes that any possible flowing water would be expected to follow. In order to address uncertainties in the bed elevation data (due to the limited resolution of the ice

thickness data from the MARSIS sensor, in particular) we adopt a similar approach to *Livingstone et al.,* [2013b] and perform a suite of lake location calculations using DEMs derived from the raw MARSIS data, the mean and median of all radar footprints crossing each point (cf. *Orosei et al.,* [2018]), and a set of 1000 DEMs interpolated from randomly perturbed bed elevation data, with perturbations calculated using the statistical properties of the elevation differences within the MARSIS data. We use different assumptions of the density of the inferred subglacial liquid, from pure water to saturated perchlorate brine, and we also investigate the impact of the spatial resolution of the interpolated DEMs. From this set of calculations we determine the most persistent predicted lake locations and predicted water flow paths. We then consider the implications of these predictions by comparing the predicted lake locations and persistence values with the high reflectance area (HRA) reported by *Orosei et al.,* [2018]. We use these predictions to consider the likelihood (or otherwise) of a well-connected subglacial drainage system beneath the Martian SPLD, or whether the possible water body inferred from radar reflectance [*Orosei et al., 2018*] is more likely to be a hydraulically-isolated feature.

2 Methods

2.1 Modeling lake locations

We calculate subglacial hydraulic potential (ϕ) from the bed and surface elevation [S*hreve*, 1972]:

$$\phi = \rho_w g Z + k \rho_i g H \quad [1]$$

where g is gravity (3.711 m s^{-2}); ρ_w is the density of the subglacial liquid, ranging from 1000 kg m^{-3} for pure water to 1980 kg m^{-3} for saturated perchlorate brine [*Fisher et al.,* 2010]; Z is the bed elevation (m), ρ_i is the ice density (here taken to be 910 kg m^{-3}, given the uncertainty concerning the overall density of the Martian SPLD; [e.g. *Zuber et al.,* 2007; *Plaut et al.,* 2007; *Wieczorek,* 2008]) and H is the ice thickness (m). k is a dimensionless factor which represents the influence of ice overburden pressure on the local subglacial water pressure, with $k = 1$ implying the water pressure is at the ice overburden pressure, and $k = 0$ implying the subglacial water is at atmospheric pressure. In terrestrial systems, k is variable in time and space, especially in situations closer to the ice margin where the ice is thinner and/or heavily affected by seasonal meltwater. In the interiors of ice sheets, where the ice is thicker, and especially for Antarctica, measured water pressures are typically very close to ice overburden. Given the location of the HRA in the interior of the SPLD, and the ~1500 m inferred ice thickness, we assume $k = 1$ in our simulations.

Equation 1 can usefully be re-cast into an alternative formulation which uses Z as before, and also the ice surface elevation, S, where $S = Z + H$:

$$\phi = (\rho_w - k \rho_i) g Z + k \rho_i g S \quad [2]$$

This alternative formulation highlights the typical dominance (for high k values) of the ice surface elevation on the subglacial hydraulic potential due to the small difference in the density of ice and water. For the SPLD, however, if the liquid layer is a high solute-concentration brine, ρ_w will be higher, increasing the importance of the basal topography in

185 determining the subglacial hydraulic potential. Given this, we use ρ_w = 1980 kg m^{-3} in the bulk
186 of our calculations, but we also perform a set of runs in which ρ_w is varied in 11 equal steps
187 between 1000 and 1980 kg m^{-3}. Uncertainty in the ice density [e.g. *Zuber et al.*, 2007; *Plaut et*
188 *al.*, 2007; *Wieczorek*, 2008] will have an opposing effect. A higher ice density will increase the
189 dominance of the ice surface elevation, reducing the role played by basal topography on the
190 subglacial potential, and reducing the impact of possible higher liquid density. If the ice density
191 exceeds the liquid density, this will reverse the sign of the first term in Eq. 2 (although this
192 negative value will be compensated to some extent by the increased value of the second term,
193 depending on the relative values of the ice and liquid densities, and the surface and bed
194 elevations). To assess the likely maximum impact of this effect, we also perform a run using an
195 ice density of 1200 kg m^{-3} [*Zuber et al.*, 2007; *Wieczorek*, 2008] and a liquid density of 1000 kg
196 m^{-3}.

197 We calculate lake locations using the flow accumulation algorithm developed by *Arnold*
198 [2010], as applied by *Willis et al.*, [2016] for Antarctica, using gridded ϕ values calculated from
199 the surface topography, inferred bed topography, and ρ_w value for each experiment. The
200 calculated hydraulic potential (hereafter shortened to potential) gradient allows inferred water
201 flow directions to be calculated for each DEM cell; the algorithm assigns each DEM cell an area,
202 based on its own area plus the total area upstream of the cell for which water flow-lines pass
203 through the cell. The algorithm also identifies all cells in the potential surface that are at a lower
204 potential than all their neighbours (and which therefore act as 'dead end' in the flow
205 accumulation algorithm) and defines them as 'sink' cells. Together, the water flow directions and
206 sink cells allow local subglacial catchments (a group of contiguous cells which all drain toward
207 the sink) to be determined. Sink cells also form the nucleus for possible subglacial lakes; the
208 algorithm 'floods' each sink cell to find the elevation of the lowest cell in the catchment
209 surrounding the sink cell over which water would spill into a lower potential downstream cell
210 (and hence, into an adjacent catchment). This spill point cell defines the maximum depth
211 (relative to the elevation of the sink cell), area, and volume of each predicted possible lake, and
212 also allows the routing algorithm to pass the total catchment area from catchment to catchment
213 downstream until the model reaches the edge of the ice cap. In this way, the algorithm builds up
214 the topology of possible subglacial water flow, linking the individual catchments and lakes
215 together into arborescent structures analogous to typical stream networks. Major drainage axes
216 appear as distinct 'threads' across the potential surface with large upstream area values, meaning
217 a large number of upstream cells ultimately feed their area through such cells. Upstream source
218 areas, or more isolated areas, show much lower upstream area values. Cells within a lake are
219 assigned an area equal to the total upstream area above the spill point for that lake. Lakes on the
220 main drainage axes appear therefore as 'beads' of high upstream area, but even lakes in upstream
221 or more isolated areas are easily identified as areas of uniform, locally-high upstream area
222 values.

223 2.2 Ice surface and bed topography

224 For the ice surface elevation, we use the south polar MOLA gridded topographic map for
225 Mars at 128 pixels per degree (460 m per pixel) resolution (Figure 1a; *Smith et al.*, [2001]) in all
226 experiments. For the bed topography, we use the MARSIS sub-spacecraft latitude and longitude,
227 and the inferred elevation of the basal reflector (used to produce the ice thickness and hence bed
228 elevation datasets from *Plaut et al.*, [2007]), supplemented with the additional data reported in

Orosei et al., [2018], to provide the x,y,z point-cloud data needed for interpolation of the bed DEMs. We perform our experiments for the 200 × 200 km area centered around 193°E, 81°S that contains the high-reflectance signal reported by *Orosei et al.,* [2018]; Figure 1b. In order to facilitate direct comparison with the results reported in Orosei et al. 2018, we also adopt a north-down orientation in Figure 1b and subsequent figures. 86 points from *Plaut et al.* [2007] fall in our study area, and allow interpolation outside the area covered by the point cloud data presented in *Orosei et al.* [2018]. In order to compare our results directly with those from *Orosei et al.,* [2018], we perform the bulk of our experiments at the 200 m resolution used by *Orosei et al.,* [2018], but we also derive DEMs at 500 m, 1000 m, 2500 m and 5000 m resolution to test the impact of DEM resolution. Following *Plaut et al.,* [2007], we use natural neighbour interpolation, and apply noise to the MARSIS data from *Orosei et al.* [2018] as detailed below for our perturbation analysis. We pin the edge of the study area to the elevation taken from the overall SPLD gridded bed elevation map [*Plaut et al.,* 2007].

The vertical resolution of the MARSIS sensor is around 100–150 m [e.g. *Plaut et al.,* 2007], controlled ultimately by the frequency and time resolution of the sensor. Inferring bed elevation from the radar returns also requires knowledge of the dielectric constant of the material; we use the values (and hence elevations) reported by *Orosei et al*. [2018]. The noise we apply to the data (detailed below) effectively allows us to simulate the impact of uncertainty in the dielectric constant however. The Fresnel radius (ground footprint) is ~3–5 km [*Orosei et al.,* 2018] and varies along-track and across-track. 76,800 individual data points are available within the study area, from 27 individual satellite tracks (Figure 2a). As can be seen in Figure 2a, however, the inferred SPLD thickness along the tracks varies considerably over quite short distances (well within the sensor footprint), which suggests that possible local variations in the dielectric, sensor resolution effects, or other noise sources strongly affect the inferred elevation. The along-track spacing of the points varies from ~30 to ~90 m, meaning that there is considerable footprint overlap along the tracks, and several sets of tracks are also close together, running nearly parallel to each other, or cross. This overlap between the footprints of the individual measurement points gives us information on the local variability or uncertainty in the inferred SPLD thickness in the MARSIS data. In order to estimate the statistical properties of this uncertainty, and provide a measure of the noise within the data, we identify all the points within the Fresnel radius of the sensor for each point, and use these to calculate the mean (Figure 2b) and median (Figure 2c) height differences, and the standard deviation (Figure 2d) of the height differences, between each original point and the other points within the Fresnel radius.

Figure 3a shows the overall distribution of in-radius elevation differences, with the calculated mean and standard deviation of height difference. It approximates a normal distribution, though with a more marked central peak. However, some individual points deviate quite markedly from their neighbours; Figure 3b-d shows the distribution for the points with the maximum (Figure 3b) and minimum (Figure 3c) mean in-radius elevation difference, and the point with the largest standard deviation (Figure 3d) of in-radius elevation difference. Of the 76,800 points, 64,496 have a standard deviation of the in-radius elevation difference smaller than ± 1 standard deviation for the total set. The number of in-radius points varies between 108 and 2362, with a mean value of 665 in-radius points per point.

We create a set of bed DEMs (shown in Figure 4 at 200 m resolution) for the hydraulic potential and flow routing calculations using the raw MARSIS points from *Orosei et al.,* [2018],

(Figure 4a); and the mean (Figure 4b), median (Figure 4c), minimum, and maximum of the elevation differences within the Fresnel radius as above. The minimum and maximum topographies were judged to be implausible due to the very large height differences produced in some areas, and are not used further. We then use a form of Monte-Carlo analysis to create a set of 1000 perturbed bed topographies by applying a random elevation change to each data point drawn from a normal distribution with the calculated mean and standard deviation of the in-radius elevation differences for that point. We apply the flow accumulation algorithm to each perturbed DEM, which then allows us to calculate a probability value that any given pixel is within a lake for the set of 1000 model runs. We also create a DEM (dubbed the mean-perturbed DEM) using the mean elevation of each cell calculated from the set of individual perturbed topographies (Figure 4d). We also apply the flow accumulation algorithm to the same set of DEMs at reduced resolution, but focus mainly on the 200 m resolution results for direct comparison with *Orosei et al.,* [2018].

Figure 4 shows that the mean, median and mean-perturbed 200 m resolution topographies are considerably smoother than that produced by the raw data. For all four, however, the impact of some of the individual satellite tracks can still be seen, such as the straight, deep trough running NNW from the S (top) edge of the area. This effect is reduced most in the mean-perturbed topography, which we therefore use in the series of experiments to investigate the possible impact of variable ρ_w values.

3 Results

Figure 5 shows the common logarithm of the flow accumulation results for the four 200 m resolution topographies shown in Figure 4, using ρ_w of 1980 kg m^{-3}.

Possible lake locations are seen as the broad patches with high, uniform flow accumulation values (yellows in Figure 5). The overall drainage trend across the majority of the area is towards the east-north-east (left/bottom left) in all four simulations, driven by the effect of the overall slope of the SPLD surface topography in the area (Figure 1b) on the subglacial hydraulic potential (Eq. 2). The effect of the surface scarps in the north-west (bottom right) of the area (Figure 1b) can also be clearly seen as the thinner ice downstream of the scarps leads to local low subglacial potential values which act as large possible lake locations. Away from the scarps, however, where the SPLD surface topography is much flatter, the basal topography acts as the major control on predicted possible lake locations. Depressions in the bed form the foci for numerous possible lakes, especially in the rougher raw topography DEM (Figure 5a). However, what is clear is that the area of high basal reflectance does not coincide with a substantial predicted possible lake location in any reconstruction.

Figure 6 shows the 2500 km^2 central area around the HRA in more detail. Consistently, three substantial possible lake locations are predicted nearly adjacent to the HRA; an irregularly shaped lake to the south-west (upper right) of the HRA; a rounder lake to the east (left), and a lake with a more variable extent to the south-east (upper left). For the raw topography DEM, several smaller lake locations are predicted within the HRA. These have lower flow accumulation values than the three larger adjacent lakes, however, and are topologically more isolated. In topological terms, the SW lake is linked to the E lake via a drainage axis running through the HRA from W to E in the mean and mean perturbed topographies (Figures 6b and d).

For the raw topography DEM (Figure 6a), the SW lake flows into the SE lake, and then to the E lake, with the predicted drainage axis touching the southern tip of the HRA. For the median topography DEM (Figure 6c), the routing is different again. The SW lake extends beyond the southern (top) edge of the study area, and flow is directed into the southern edge of the SE lake (outside the area shown in the figure), and then to the E lake; no substantial drainage axis crosses the HRA.

Figure 7a shows the probability values (P) for whether any given pixel is part of a possible lake from the set of 1000 perturbed topography runs. P is calculated by dividing the number of runs in which a pixel is calculated to be within a lake by the total number of runs. Thus, P = 0 for a pixel which was never calculated to be in a lake and P = 1 for a pixel which was calculated to be in a lake in all simulations. Here, the overall position of the three large adjacent predicted possible lakes is robust to perturbation using the calculated elevation variation statistics, although their exact extents vary (with the edges of the lakes having lower pixel probabilities), particularly for the southern extent of the SW lake. A small but persistent lake also appears in the southern part of the HRA that is less apparent in the single topography calculations (Figures 5 and 6). The individual satellite tracks are visible, as small predicted possible lakes will form in some topographies when an individual point is randomly moved downwards by a large amount, producing a deep, small depression, or when nearby points are moved upwards producing a depression between them. Figure 7b shows the mean flow accumulation values for the 1000 perturbed-topography runs. This again shows the persistence of the main predicted possible lakes; the lake edges are less sharp than for the single-topography runs, as pixels nearer the margins which are only calculated to be in lakes in some perturbed topographies will have lower mean flow accumulation values. There is also some blurring of the main drainage axes as calculated routing between the lakes will vary between the different perturbed topographies, but again, a drainage axis running W-E across the southern part of the HRA is visible, as occurs in the mean and mean-perturbed topographies (Figures 5 and 6b and d).

Figures 7c–f show the results for the variable liquid and ice density experiments. Figure 7c shows the probability that any given pixel is part of a lake and Figure 7d shows the mean flow accumulation values for the 11 variable liquid density runs. Figure 7e shows the results for the ρ_w = 1000 kg m^{-3} run, and Figure 7f the results for the ρ_i = 1200 kg m^{-3} and ρ_w =1000 kg m^{-3} run. As implied by Eq. 2, for lower-density liquid the impact of bed topography is heavily reduced, and the surface slope dominates. For ρ_w = 1000 kg m^{-3}, calculated lake occurrence in the vicinity of the HRA is virtually eliminated (Figure 7e). As liquid density increases, the SE lake begins to form at the lowest liquid density, and increases in extent most rapidly, as shown by the largest area of high probability (Figure 7c) and the largest area of high (bright yellow) mean flow accumulation values (Figure 7d). The SW and E lakes only become more extensive for inferred density > ~1600 kg m^{-3}, with smaller areas of high probability (Figure 7c) and high mean flow accumulation values (Figure 7d). The drainage axis from the SW to E lake through the HRA is present in all variable-density runs (Figure 7d). For the run with ρ_i = 1200 kg m-3 and ρ_w =1000 kg m-3 (Figure 7f), the overall pattern of flow is similar to the ρ_w = 1000 kg m^{-3} run (Figure 7e) particularly within the HRA, which shows no predicted lake occurrence. The small predicted lake upstream of the location of the SE lake is caused by the increased impact of the thicker ice over the deep bed depression in this area preventing water from being routed through the depression, forcing water to flow around the bed depression.

Figure 8 shows the mean flow accumulation values from the set of 1000 reduced resolution perturbed-topography runs (the equivalent to the 200 m resolution results shown in Figure 7b). These clearly show that resolution does not affect the location of the predicted possible lakes, nor the route of the drainage axis from the SW to E lake through the HRA. Only at the coarsest resolution (5000 m, Figure 8d) does the pattern start to break down somewhat, with the SW and E lakes remaining as separate entities, but linked by a much broader drainage axis through the HRA.

4 Discussion

Mapping the locations of depressions in subglacial hydraulic potential surfaces has proved very successful in terms of predicting the location of subglacial lakes and drainage axes on Earth. The robust results reported here, which show that the HRA beneath the SPLD does not occupy such a depression, but occurs within 10 to 20 km of three such possible depressions which do not show high radar reflectances [Orosei et al. 2018], therefore seems anomalous. However, there are critical differences between the vast majority of terrestrial subglacial lakes and a hypothesized lake (or area of basal liquid) beneath the SPLD. Almost all known subglacial lakes on Earth are fed by meltwater which flows into the lake basin from upstream, delivered by an active subglacial drainage system that covers the ice sheet bed, which is at the pressure melting point, over wide areas. For Antarctica, where large numbers of subglacial lakes are known to exist, the main water source is basal melt. Numerical modeling suggests mean subglacial melt rates around 2–5 mm yr^{-1} beneath Antarctica, with some fast flowing areas reaching several hundred mm per year [e.g. *Willis et al.,* 2016; *Pattyn* 2010, *Llubes et al.,* 2006]. Basal melt is generated by a combination of strain heating and geothermal heat flux; West Antarctica in particular exhibits some of the highest melt rates, as it is thought to have relatively high geothermal heat flux of over 120 mW m^{-2} in places (versus a continent-wide average value of 30-60 mW m^{-2}) [*Martos et al.,* 2017], and contains areas of very fast-moving ice which generate large amounts of strain heating. These high basal melt rates lead to sometimes very substantial water fluxes [over 1 km^3 yr^{-1}, *Willis et al.,* 2016] into some active lakes near the margins of Antarctica, which can trigger cyclic drainage events which have been observed through their impact on the surface topography of the ice sheet [e.g. *Wingham et al.,* 2006, *Fricker et al.,* 2007]. Such conditions are therefore very different from those at the base of the SPLD.

As well as subglacial lakes with large catchments fed by near-ubiquitous basal melt (such as beneath Antarctica), subglacial lakes directly fed by localized high geothermal heat fluxes are known to exist on Earth. The most widely studied is Grimsvötn, a subglacial lake beneath Vatnajökull, a large ice cap in SW Iceland. This lake is known to fill due to subglacial melt driven by very high geothermal heating [estimated at 35–40 W m^{-2}, *Björnsson and Guðmundsson*, 1993], and then drain catastrophically when the lake volume exceeds a threshold. Subglacial hydrological theory has proved rather successful at predicting the discharge hydrographs of these drainage events [e.g. *Nye*, 1976; *Spring and Hutter*, 1981, *Fowler*, 1999], and even (though with less certainty) the triggers of the drainage events [*Fowler*, 1999]. The key finding from Grimsvötn is that the lake forms in a topographic depression beneath the ice, which causes a low in the subglacial hydraulic potential. The lake surface, however, can reach a higher elevation than the top of the topographic lip of the basin as the subglacial potential increases in front of the lake due to thicker ice downstream. This reversed potential slope impounds the lake,

not the bed topography in itself. At some critical water level, however, the potential gradient reverses and the lake drains catastrophically, as the large water discharge enables rapid growth of an efficient subglacial drainage system. These drainage events result in catastrophic floods (jökulhlaups) beyond the ice cap margin, and result in the formation of pronounced cauldrons on the ice cap surface.

Figure 9 shows the surface and basal topography, and subglacial hydraulic potential, for a transect through the HRA located on the drainage axis between the SW and E depressions beneath the SPLD (shown in Figure 7b). The reverse gradient in subglacial potential that impounds the two predicted lakes can be clearly seen, but no such reverse gradient exists for the region occupied by the HRA.

In addition to local melt, Grimsvötn is thought to also receive melt from upstream [e.g. *Fowler*, 1999]; the ice cap is also at the pressure melting point, so once discharge from the lake is underway, no thermal barrier exists to prevent drainage. This also contrasts strongly with the situation beneath the SPLD. If locally-raised geothermal heating is necessary to raise the basal ice to the melting point [*Sori and Bramson*, 2019], the rate of filling of any putative lake would be far slower. This is because of the lower likely geothermal heating, more rapid loss of heat through the much colder ice within the SPLD, and the lack of any upstream catchment to feed additional melt into the hypothesized lake. The inferred liquid beneath the SPLD therefore seems to be trapped by a thermal 'dam', rather than by variations in the potential surface. This perhaps makes it less likely that the HRA is a true subglacial lake, in the sense of being constrained by topography.

The geophysical model results presented by *Sori and Bramson* [2019] show geothermal heating rising rapidly (over ~0.5 Myr) after the intrusion of a magma chamber beneath the HRA, and then falling more slowly (over the subsequent 1–2 Myr). If the HRA is indeed geothermally-heated liquid, it could therefore currently be on the 'rising limb' of heating, and getting larger; at its peak extent (though perhaps this is the least likely scenario due to the shorter duration of peak heating); or on the 'falling limb', and shrinking. If the former is the case, and the extent of basal melt increases in the future such that the area expands to encompass our predicted depressions in the potential surface, then we can speculate whether such an occurrence would allow a 'true' subglacial lake, pinned by the topography, to form. We can also speculate if a rapid drainage event of this lake would occur if it reached some critical volume threshold. In the latter case, and especially if a drainage event had occurred in the past, it could be the case that some topographic signature on the surface of the SPLD might be manifest. Whilst Icelandic subglacial volcanism can produce cauldrons several hundred meters deep for ice typically up to ~500 m thick, numerical modeling [e.g. *Evatt and Fowler*, 2007] and observations [e.g. *Wingham et al.*, 2006, *Fricker et al.*, 2007, 2009] suggest changes in surface topography of a few metres for lakes of similar size to the HRA for the thicker ice, and pressure-driven drainage events, known to occur for Antarctic subglacial lakes. Such topographic signatures would be difficult to detect on the SPLD, but could perhaps be detected in derivatives of the highest resolution MOLA elevation data. Currently no such anomalous topography can be discerned on the ice surface over the HRA.

Our results do not suggest that the explanation of the HRA being caused by the presence of liquid water [*Orosei et al.*, 2018] is any more or less likely due to it not being in a depression

447 within the calculated subglacial potential surface. Our results also suggest that spatially-limited
448 geothermal heating seems unlikely to produce an active subglacial drainage system capable of
449 sustaining flow across parts of the bed, but rather that spatially-limited heating may produce melt
450 which is pinned *in-situ* by the surrounding frozen base. This suggests that more extensive basal
451 melting, driven by a combination of a larger area of higher geothermal heating, thicker ice and
452 warmer surface temperatures (all of which were more probable earlier in Mars' history, and in
453 agreement with previous palaeo-environmental reconstructions [e.g. *Fastook et al*., 2012;
454 *Scanlon et al.,* 2018]), would be required for the occurrence of an active subglacial drainage
455 system capable of moving large quantities of sediment, and therefore of forming the ancient
456 [~3.5–3.6 Ga; *Kress and Head* 2015; *Bernhardt et al.,* 2013] putative eskers in the south polar
457 Dorsa Argentea Formation and Argyre Planitia [e.g., *Butcher et al.,* 2016; *Bernhardt et al.,*
458 2013]. In the case of the younger (110–150 Ma) esker systems observed in Mars' mid-latitudes
459 [*Gallagher and Balme,* 2015, *Butcher et al.,* 2017], however, widespread subglacial melt seems
460 less likely given the colder Martian climate in the Amazonian. Mid-latitude glaciers are thought
461 to have been more extensive during periods of high obliquity, however [e.g. *Baker and Head*
462 2015], which would tend to warm the basal ice directly, and could lead to higher strain heating
463 due to larger basal shear stress [*Butcher et al.,* 2017]. Coupled with locally elevated geothermal
464 heat, this would make it more likely for the basal ice to reach the melting point in the area above
465 the geothermal anomaly, especially if salts lowered the melting point of the basal ice. Were the
466 melting to occur over a large enough area, this liquid might begin to flow down the potential
467 surface or become impounded in depressions in the subglacial hydraulic potential surface as
468 topographically-constrained subglacial lakes. The number and extent of such depressions in the
469 potential surface would be increased if the basal liquid consisted of high-density brine. The
470 possible growth of any such lakes during the onset-to-peak phase of heating could lead to them
471 filling the depressions in the potential surface, possibly reaching the threshold size needed for
472 catastrophic drainage to occur. This would seem likely to mobilise large quantities of sediment,
473 leading to possible esker formation in a transient subglacial drainage system. Such a mechanism
474 could help explain the occurrence, size, and also the rarity, of modern mid-latitude Martian
475 eskers.

476 **5 Conclusions**

477 Our results show that the HRA reported by *Orosei et al.,* [2108] beneath the Martian
478 SPLD does not occupy a depression in the subglacial hydraulic potential surface as calculated
479 using subglacial hydraulic theory and the surface and basal topographies. This finding is robust
480 to random perturbations of the bed DEM using the mean and standard deviation of elevation
481 difference (calculated from the set of points within the Fresnel radius for each point), to different
482 interpolation resolutions, and to different assumed densities for the inferred liquid layer. For the
483 latter case, a higher assumed density increases the effect of the bed topography on the subglacial
484 potential surface, as expected from subglacial hydraulic potential theory (Eq. 2, *Shreve*, [1972]),
485 and makes predicted lake locations both larger in extent, and more numerous. Three substantial
486 depressions in the potential surface, with areas between one-third and three-quarters of the area
487 of HRA, are predicted to occur within ~20 km of the HRA, and a major drainage axis in the
488 potential surface crosses the HRA in over 90% of the perturbed topographies, a topography
489 calculated using the mean in-radius elevation, and a topography calculated from the mean
490 elevation of the set of 1000 perturbed topographies. The areas occupied by these depressions do

not show high radar reflectance in the MARSIS data, and therefore show no sign of liquid water [*Orosei et al. 2018*].

The methodology we develop here to acknowledge the uncertainty in radar-derived bed elevation data adds confidence to our findings. Flow accumulation calculations require the gradient in the bed elevation to be calculated, and as such are very sensitive to noise in the point-cloud data used to produce interpolated DEMs. Assessing the local variation in the inferred topography using the inherent spatial overlap between the individual sensor measurements (given the large footprint on the MARSIS instrument relative to the measurement frequency) allows us to calculate the statistical properties of the bed elevation estimates around each original point, and hence of the uncertainties in the estimated bed elevation. These statistics then allow realistic random noise values to be added to the point-cloud data in a form of Monte-Carlo analysis, which allows the calculation of both the mean elevation of pixels in the individual perturbed topographies, and the mean values from any analysis using the individual perturbed topographies. For analyses that require the gradient of the topography to be calculated, this procedure adds valuable robustness to the calculated values.

We suggest that if the HRA is due to the presence of liquid water, or at least water-saturated basal sediments, the location of the HRA seems likely to be due to locally-forced in-situ basal melting, rather than the melt occurring elsewhere and the resulting liquid then collecting in an area of low hydraulic potential as is typical for terrestrial subglacial lakes. This supports the argument made by *Sori and Bramson* [2019] that localized geothermal heating is the heat source required for melt to occur. Given that the subglacial potential surface in the HRA does not show any substantial depressions, but instead seems to include a major predicted drainage axis, the area of inferred basal melt seems to be pinned in-situ, presumably by the surrounding cold-based ice which acts as an effective aquiclude and prevents movement of the liquid down the subglacial potential surface. We suggest that the HRA does not represent a ‘true’ subglacial lake, pinned by topography, but that if it does represent liquid water, it is more likely to be a brine-enriched sludge, or to consist of shallow (but spatially extensive) brine pools as suggested by *Orosei et al.* [2018].

Acknowledgments

The MARSIS instrument and experiment were funded by the Italian Space Agency and NASA. It was developed by the University of Rome, Italy, in partnership with NASA's Jet Propulsion Laboratory [JPL], Pasadena, CA. The Mars Express and Mars Global Surveyor missions are operated by the space agencies of the United States (NASA), Europe (European Space Agency) and Italy (Agenzia Spaziale Italiana). We particularly thank Roberto Orosei for providing the raw MARSIS data, including the inferred elevation of the basal reflector, used in *Orosei et al*., [2018]. Parts of this work were undertaken whilst FEGB was in receipt of a UK STFC funded PhD studentship, grant number ST/N50421X/1. The authors declare no competing interests. Code and derived data developed during this research are available at: https://doi.org/10.17863/CAM.41622. MARSIS data used in this study are available in the repository maintained by *Orosei et al.* [2018] at http://doi.org/10.5281/zenodo.1285179. MOLA data are available from the PDS Geosciences node at: http://pds-geosciences.wustl.edu/missions/mgs/megdr.html.

References

Arfstrom, J., & Hartmann, W. K. (2005). Martian flow features, moraine-like ridges, and gullies: Terrestrial analogs and interrelationships. *Icarus*, *174*(2), 321–335. https://doi.org/10.1016/j.icarus.2004.05.026

Arnold, N. (2010). A new approach for dealing with depressions in digital elevation models when calculating flow accumulation values. *Progress in Physical Geography: Earth and Environment*, *34*(6), 781–809. https://doi.org/10.1177/0309133310384542

Baker, D. M. H., & Head, J. W. (2015). Extensive Middle Amazonian mantling of debris aprons and plains in Deuteronilus Mensae, Mars: Implications for the record of mid-latitude glaciation. *Icarus*, *260*, 269–288. https://doi.org/10.1016/j.icarus.2015.06.036

Bernhardt, H., Hiesinger, H., Reiss, D., Ivanov, M., & Erkeling, G. (2013). Putative eskers and new insights into glacio-fluvial depositional settings in southern Argyre Planitia, Mars. *Planetary and Space Science*, *85*, 261–278. https://doi.org/10.1016/j.pss.2013.06.022

Björnsson, H., & Guðmundsson, M. T. (1993). Variations in the thermal output of the subglacial Grímsvötn Caldera, Iceland. *Geophysical Research Letters*, *20*(19), 2127–2130. https://doi.org/10.1029/93GL01887

Bramson, A. M., Byrne, S., & Bapst, J. (2017). Preservation of Midlatitude Ice Sheets on Mars: Mars Midlatitude Ice Sheet Preservation. Journal of Geophysical Research: Planets, 122(11), 2250–2266. https://doi.org/10.1002/2017JE005357

Butcher, F. E. G., Conway, S. J., & Arnold, N. S. (2016). Are the Dorsa Argentea on Mars eskers? *Icarus*, *275*, 65–84. https://doi.org/10.1016/j.icarus.2016.03.028

Butcher, F. E. G., Balme, M. R., Gallagher, C., Arnold, N. S., Conway, S. J., Hagermann, A., & Lewis, S. R. (2017). Recent basal melting of a mid-latitude glacier on Mars. *Journal of Geophysical Research: Planets*, *122*(12), 2445–2468. https://doi.org/10.1002/2017JE005434

Clark, C. D., Ely, J. C., Greenwood, S. L., Hughes, A. L. C., Meehan, R., Barr, I. D., et al. (2018). BRITICE Glacial Map, version 2: a map and GIS database of glacial landforms of the last British-Irish Ice Sheet. *Boreas*, *47*(1), 11-e8. https://doi.org/10.1111/bor.12273

Conway, S. J., Butcher, F. E. G., de Haas, T., Deijns, A. A. J., Grindrod, P. M., & Davis, J. M. (2018). Glacial and gully erosion on Mars: A terrestrial perspective. *Geomorphology*, *318*, 26–57. https://doi.org/10.1016/j.geomorph.2018.05.019

Evatt, G. W., & Fowler, A. C. (2007). Cauldron subsidence and subglacial floods. *Annals of Glaciology*, *45*, 163–168. https://doi.org/10.3189/172756407782282561

Fassett, C. I., Dickson, J. L., Head, J. W., Levy, J. S., & Marchant, D. R. (2010). Supraglacial and proglacial valleys on Amazonian Mars. *Icarus*, *208*(1), 86–100. https://doi.org/10.1016/j.icarus.2010.02.021

Fastook, J. L., Head, J. W., Marchant, D. R., & Forget, F. (2008). Tropical mountain glaciers on Mars: Altitude-dependence of ice accumulation, accumulation conditions, formation times, glacier dynamics, and implications for planetary spin-axis/orbital history. Icarus, 198(2), 305–317. https://doi.org/10.1016/j.icarus.2008.08.008

Fastook, J. L., Head, J. W., Marchant, D. R., Forget, F., & Madeleine, J.-B. (2012). Early Mars climate near the Noachian–Hesperian boundary: Independent evidence for cold conditions from basal melting of the south polar ice sheet (Dorsa Argentea Formation) and implications for valley network formation. *Icarus*, *219*(1), 25–40.

https://doi.org/10.1016/j.icarus.2012.02.013
Fisher, D. A., Hecht, M. H., Kounaves, S. P., & Catling, D. C. (2010). A perchlorate brine lubricated deformable bed facilitating flow of the north polar cap of Mars: Possible mechanism for water table recharging. *Journal of Geophysical Research*, *115*, E00E12, https://doi.org/10.1029/2009JE003405
Flowers, G. E. (2015). Modelling water flow under glaciers and ice sheets. *Proceedings of the Royal Society A: Mathematical, Physical and Engineering Sciences*, *471*(2176), 20140907–20140907. https://doi.org/10.1098/rspa.2014.0907
Fowler, A. C. (1999). Breaking the seal at Grímsvötn, Iceland. *Journal of Glaciology*, *45*(151), 506–516. https://doi.org/10.1017/S0022143000001362
Fricker, H. A., & Scambos, T. (2009). Connected subglacial lake activity on lower Mercer and Whillans Ice Streams, West Antarctica, 2003–2008. *Journal of Glaciology*, *55*(190), 303–315. https://doi.org/10.3189/002214309788608813
Fricker, H. A., Scambos, T., Bindschadler, R., & Padman, L. (2007). An active subglacial water system in West Antarctica mapped from space. *Science*, *315*(5818), 1544–1548. https://doi.org/10.1126/science.1136897
Gallagher, C., & Balme, M. (2015). Eskers in a complete, wet-based glacial system in the Phlegra Montes region, Mars. *Earth and Planetary Science Letters*, *431*, 96–109. https://doi.org/10.1016/j.epsl.2015.09.023
Head, J. W., Mustard, J. F., Kreslavsky, M. A., Milliken, R. E., & Marchant, D. R. (2003). Recent ice ages on Mars. *Nature*, *426*(6968), 797–802. https://doi.org/10.1038/nature02114
Kress, A. M., & Head, J. W. (2015). Late Noachian and early Hesperian ridge systems in the south circumpolar Dorsa Argentea Formation, Mars: Evidence for two stages of melting of an extensive late Noachian ice sheet. *Planetary and Space Science*, *109–110*, 1–20. https://doi.org/10.1016/j.pss.2014.11.025
Le Brocq, A. M., Payne, A. J., Siegert, M. J., & Alley, R. B. (2009). A subglacial water-flow model for West Antarctica. *Journal of Glaciology*, *55*(193), 879–888. https://doi.org/10.3189/002214309790152564
Levy, J. S., Fassett, C. I., Head, J. W., Schwartz, C., & Watters, J. L. (2014). Sequestered glacial ice contribution to the global Martian water budget: Geometric constraints on the volume of remnant, midlatitude debris-covered glaciers. *Journal of Geophysical Research: Planets*, *119*(10), 2188–2196. https://doi.org/10.1002/2014JE004685
Levy, J. S., Fassett, C. I., & Head, J. W. (2016). Enhanced erosion rates on Mars during Amazonian glaciation. *Icarus*, *264*, 213–219. https://doi.org/10.1016/j.icarus.2015.09.037
Livingstone, S. J., Clark, C. D., & Tarasov, L. (2013a). Modelling North American palaeo-subglacial lakes and their meltwater drainage pathways. *Earth and Planetary Science Letters*, *375*, 13–33. https://doi.org/10.1016/j.epsl.2013.04.017
Livingstone, S. J., Clark, C. D., Woodward, J., & Kingslake, J. (2013b). Potential subglacial lake locations and meltwater drainage pathways beneath the Antarctic and Greenland ice sheets. *The Cryosphere*, *7*(6), 1721–1740. https://doi.org/10.5194/tc-7-1721-2013
Llubes, M., Lanseau, C., & Rémy, F. (2006). Relations between basal condition, subglacial hydrological networks and geothermal flux in Antarctica. *Earth and Planetary Science Letters*, *241*(3–4), 655–662. https://doi.org/10.1016/j.epsl.2005.10.040
Martos, Y. M., Catalán, M., Jordan, T. A., Golynsky, A., Golynsky, D., Eagles, G., & Vaughan, D. G. (2017). Heat Flux Distribution of Antarctica Unveiled. *Geophysical Research*

Letters, *44*(22), 11,417–11,426. https://doi.org/10.1002/2017GL075609

Nye, J. F. (1976). Water flow in glaciers: jökulhlaups, tunnels and veins. *Journal of Glaciology*, *17*(76), 181–207. https://doi.org/10.1017/S002214300001354X

Orosei, R., Lauro, S. E., Pettinelli, E., Cicchetti, A., Coradini, M., Cosciotti, B., et al. (2018). Radar evidence of subglacial liquid water on Mars. *Science*, eaar7268. https://doi.org/10.1126/science.aar7268

Pattyn, F. (2010). Antarctic subglacial conditions inferred from a hybrid ice sheet/ice stream model. *Earth and Planetary Science Letters*, *295*(3–4), 451–461. https://doi.org/10.1016/j.epsl.2010.04.025

Plaut, J. J., Picardi, G., Safaeinili, A., Ivanov, A. B., Milkovich, S. M., Cicchetti, A., et al. (2007). Subsurface radar sounding of the south polar layered deposits of Mars. *Science*, *316*(5821), 92–95. https://doi.org/10.1126/science.1139672

Scanlon, K. E., Head, J. W., Fastook, J. L., & Wordsworth, R. D. (2018). The Dorsa Argentea Formation and the Noachian-Hesperian climate transition. *Icarus*, *299*, 339–363. https://doi.org/10.1016/j.icarus.2017.07.031

Shreve, R. L. (1972). Movement of water in glaciers. *Journal of Glaciology*, *11*(62), 205–214. https://doi.org/10.1017/S002214300002219X

Shreve, R.L., 1985. Late Wisconsin ice-surface profile calculated from Esker paths and types. Katahdin Esker System, Maine. *Quaternary Research* 23, 27–37. https://doi.org/10.1016/0033-5894(85)90069-9.

Smith, D. E., Zuber, M. T., Frey, H. V., Garvin, J. B., Head, J. W., Muhleman, D. O., et al. (2001). Mars Orbiter Laser Altimeter: Experiment summary after the first year of global mapping of Mars. *Journal of Geophysical Research: Planets*, *106*(E10), 23689–23722. https://doi.org/10.1029/2000JE001364

Sori, M. M., & Bramson, A. M. (2019). Water on Mars, with a grain of salt: local heat anomalies are required for basal melting of ice at the south pole today. *Geophysical Research Letters*, *46*(3), 1222–1231. https://doi.org/10.1029/2018GL080985

Souness, C., & Hubbard, B. (2012). Mid-latitude glaciation on Mars. *Progress in Physical Geography: Earth and Environment*, *36*(2), 238–261. https://doi.org/10.1177/0309133312436570

Spring, U., & Hutter, K. (1981). Numerical studies of Jökulhlaups. *Cold Regions Science and Technology*, *4*(3), 227–244. https://doi.org/10.1016/0165-232X(81)90006-9

Storrar, R. D., Stokes, C. R., & Evans, D. J. A. (2013). A map of large Canadian eskers from Landsat satellite imagery. *Journal of Maps*, *9*(3), 456–473. https://doi.org/10.1080/17445647.2013.815591

Stroeven, A. P., Hättestrand, C., Kleman, J., Heyman, J., Fabel, D., Fredin, O., et al. (2016). Deglaciation of Fennoscandia. *Quaternary Science Reviews*, *147*, 91–121. https://doi.org/10.1016/j.quascirev.2015.09.016

Tanaka, K.L., Skinner, J.A., Jr., Dohm, J.M., Irwin, R.P., III, Kolb, E.J., Fortezzo, C.M., Platz, T., Michael, G.G., and Hare, T.M., (2014), Geologic map of Mars: U.S. Geological Survey Scientific Investigations Map 3292, scale 1:20,000,000, pamphlet 43 p., http://dx.doi.org/10.3133/sim3292

Wieczorek, M. (2008). Constraints on the composition of the Martian south polar cap from gravity and topography. *Icarus*, *196*(2), 506–517. https://doi.org/10.1016/j.icarus.2007.10.026

Willis, I. C., Pope, E. L., Leysinger Vieli, G. J.-M. C., Arnold, N. S., & Long, S. (2016).

671 Drainage networks, lakes and water fluxes beneath the Antarctic ice sheet. *Annals of*
672 *Glaciology*, *57*(72), 96–108. https://doi.org/10.1017/aog.2016.15
673 Wingham, D. J., Siegert, M. J., Shepherd, A., & Muir, A. S. (2006). Rapid discharge connects
674 Antarctic subglacial lakes. *Nature*, *440*(7087), 1033–1036.
675 https://doi.org/10.1038/nature04660
676 Wordsworth, R., Forget, F., Millour, E., Head, J. W., Madeleine, J.-B., & Charnay, B. (2013).
677 Global modelling of the early Martian climate under a denser CO_2 atmosphere: Water
678 cycle and ice evolution. *Icarus*, *222*(1), 1–19.
679 https://doi.org/10.1016/j.icarus.2012.09.036
680 Wright, A. P., Siegert, M. J., Le Brocq, A. M., & Gore, D. B. (2008). High sensitivity of
681 subglacial hydrological pathways in Antarctica to small ice-sheet changes. *Geophysical*
682 *Research Letters*, *35*(17). https://doi.org/10.1029/2008GL034937
683 Zuber, M. T., Phillips, R. J., Andrews-Hanna, J. C., Asmar, S. W., Konopliv, A. S., Lemoine, F.
684 G., et al. (2007). Density of Mars' south polar layered deposits. *Science*, *317*(5845),
685 1718–1719. https://doi.org/10.1126/science.1146995
686
687

Figure Captions

Figure 1. **a**. Map of the SPLD, showing the region containing the HRA argued to be subglacial liquid by *Orosei et al.*, [2018]. The surface topography is taken from the MOLA topographic dataset [*Smith et al.*, 2001]. The black contour shows the outline of the late Amazonian polar cap (lApc) unit [*Tanaka et al.*, 2014]; the black square delineates the area investigated in *Orosei et al.*, [2018], and which we investigate in this study. **b**. MOLA surface topography of the study area highlighted by the black square in a. The red contour shows the location of the HRA reported by *Orosei et al.*, [2018]. Color scale for both maps shows MOLA elevation in m; X and Y axes in B are distances in km from the center of the study area.

Figure 2. MARSIS points for the 200 × 200 km area containing the HRA (red contour) reported by *Orosei et al.*, [2018], shown in Figure 1. **a**. Unadjusted (raw) bed elevation (m). **b**-**d**. Mean (**b**), median (**c**) and standard deviation (**d**) of elevation difference (m) between each point and the set of points within the sensor Fresnel radius. X and Y axis units are km from the center of the area; color scale units are meters. Dots are scaled to the Fresnel radius of ~4 km.

Figure 3. Frequency distributions of the elevation differences for each point and its neighbours within the Fresnel radius for that point. **a**. Overall distribution for all points. **b**. The point with the maximum mean elevation difference. **c**. The point with the minimum mean elevation difference. **d**. The point with the maximum standard deviation of elevation difference. X axis units are meters of elevation difference; Y axis units are point counts. Red line shows the best-fit normal distribution.

Figure 4. Gridded 200 m topography of study area sub-ice bed based on: **a**. raw MARSIS radar data (Figure 2a, *Orosei et al.*, [2018]; **b**-**c**: mean (**b**) and median (**c**) elevation of all points in the Fresnel radius of each original point (Figure 2b-c); **d**. mean elevation of the 1000 perturbed topographies (see text). X and Y axis units are km from the center of the area; color scale shows elevation in meters. The red contour shows the HRA reported by *Orosei et al.*, [2018].

Figure 5. Calculated flow accumulation values at 200 m resolution for: **a**. Interpolated raw topography. **b**. Mean in-radius topography. **c**. Median in-radius topography. **d**. Mean-perturbed topography (see text). X and Y axis units are km from the center of the area; color scale units are the common logarithm of the upstream area flowing into each cell in km^2. The red contour shows the HRA reported by *Orosei et al.*, [2018].

Figure 6. Calculated flow accumulation grids at 200 m resolution for the central region around the HRA: **a**. Interpolated raw topography. **b**. Mean in-radius topography. **c**. Median in-radius topography. **d**. Mean-perturbed topography (see text). X and Y axis units are km from the center of the area; color scale units are the common logarithm of the upstream area flowing into each cell in km^2. The red contour shows the HRA reported by *Orosei et al.*, [2018].

Figure 7. **a-b**. Results of the 1000 perturbed-topography experiments at 200 m resolution **a**. Probability value that any given DEM cell is within a lake for the set of 1000 perturbed-topography runs. **b**. Mean upstream area for the flow accumulation algorithm results. **c-f**. Results of the variable liquid and ice density experiments using the 200 m mean-perturbed topography (shown in Figure 4d). **c**. Probability value that any given DEM cell is within a lake for the

variable liquid density experiments. **d**. Mean upstream area for the flow accumulation algorithm runs. **e**. Calculated flow accumulation grid for the ρ_w = 1000 kg m^{-3} experiment with standard ρ_i. **f**. Calculated flow accumulation grid for the ρ_i = 1200 kg m^{-3}, ρ_w = 1000 kg m^{-3} experiment. Color scale units for a and c are probability values; P = 0 shows a pixel was never calculated to be in a lake; P = 1 shows a pixel was calculated to be in a lake in all simulations. Color scale units for b, d, e and f are the common logarithm of the upstream area flowing into each cell in km^2. X and Y axis units are km from the center of the area. The red contour shows the HRA reported by *Orosei et al.,* [2018]. Black line labeled X–Y in Panel B shows the location of the transect shown in Figure 9.

Figure 8. Mean upstream area for the set of 1000 reduced resolution perturbed topography runs. **a**. 500 m resolution. **b**. 1000 m resolution. **c**. 2500 m resolution. **d**. 5000 m resolution. Color scale units are the common logarithm of the upstream area flowing into each cell in km^2. X and Y axis units are km from the center of the area. The red contour shows the HRA reported by *Orosei et al.,* [2018].

Figure 9. Cross-section through the HRA along transect X–Y shown in Figure 7b. Basal topography is from the 200 m mean-perturbed DEM. The black arrow shows the extent of the HRA. Note the discontinuity in the left-hand Yaxis to improve visibility of the basal topography.

Figure 1.

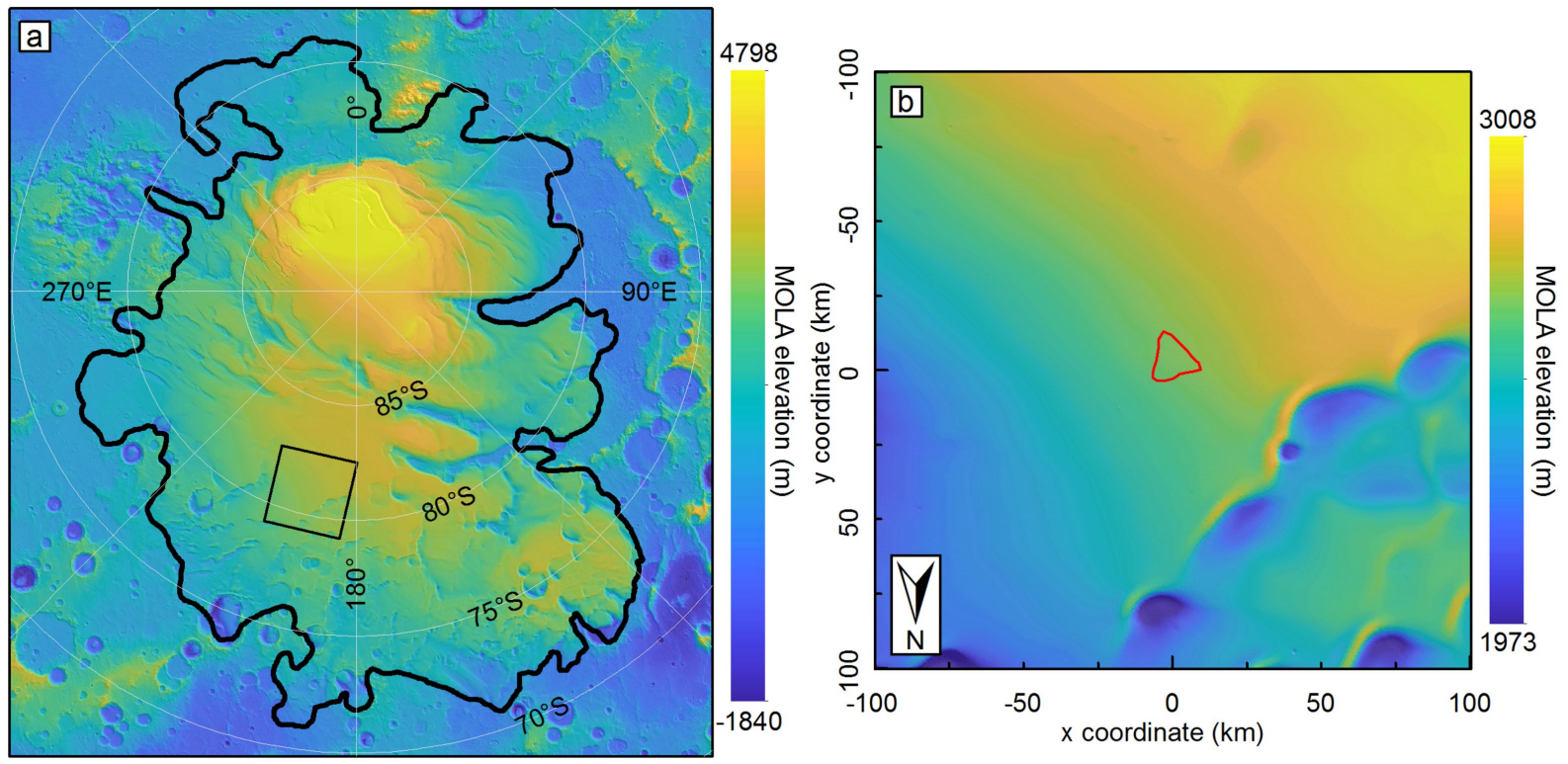
a
0°
270°E
90°E
85°S
80°S
180°
75°S
70°S
4798
MOLA elevation (m)
-1840
b
-100
-50
0
50
100
y coordinate (km)
x coordinate (km)
N
3008
MOLA elevation (m)
1973

Figure 2.

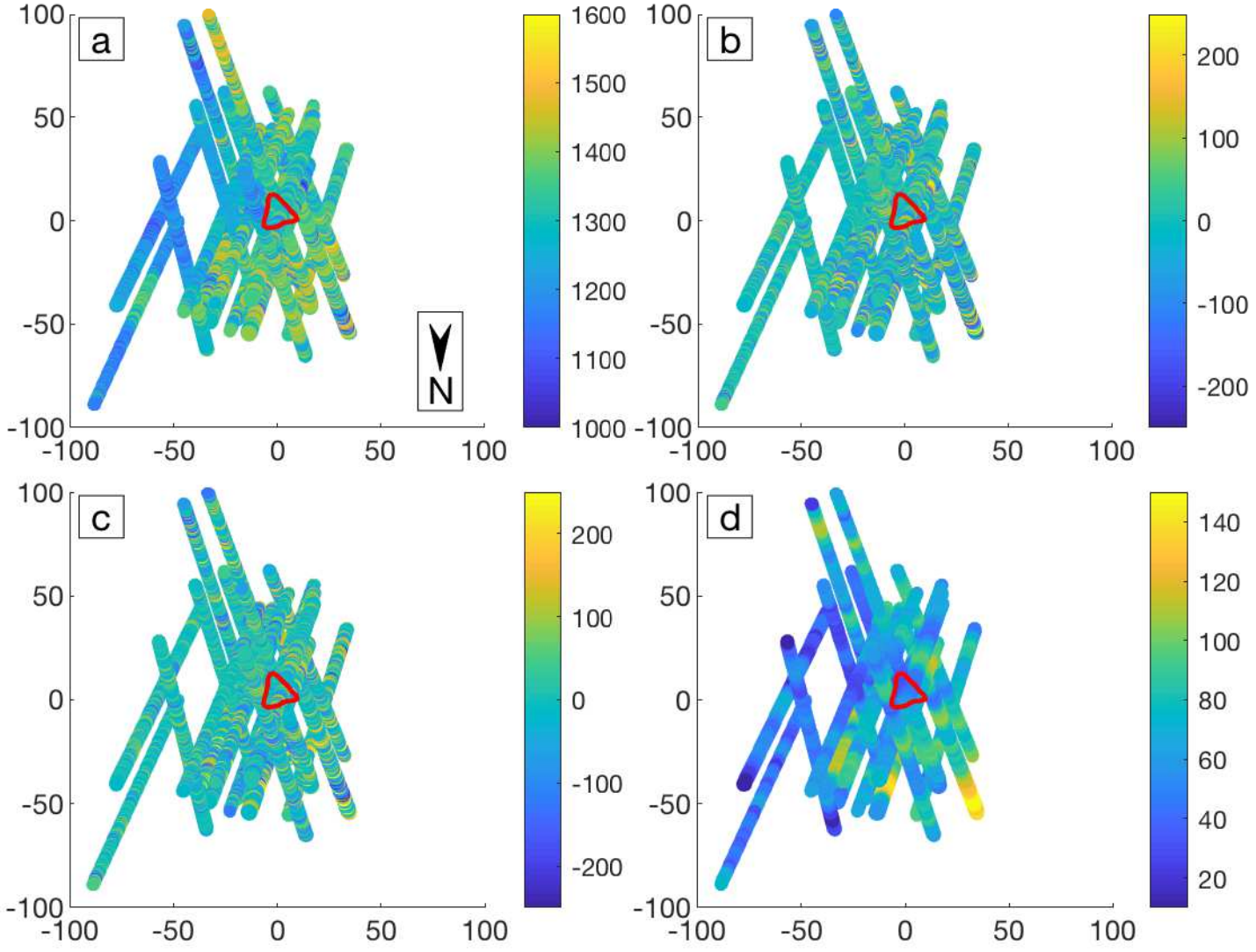
a
b
c
d
N
100
50
0
-50
-100
-100
-50
0
50
100
1600
1500
1400
1300
1200
1100
1000
200
100
0
-100
-200
140
120
100
80
60
40
20

Figure 3.

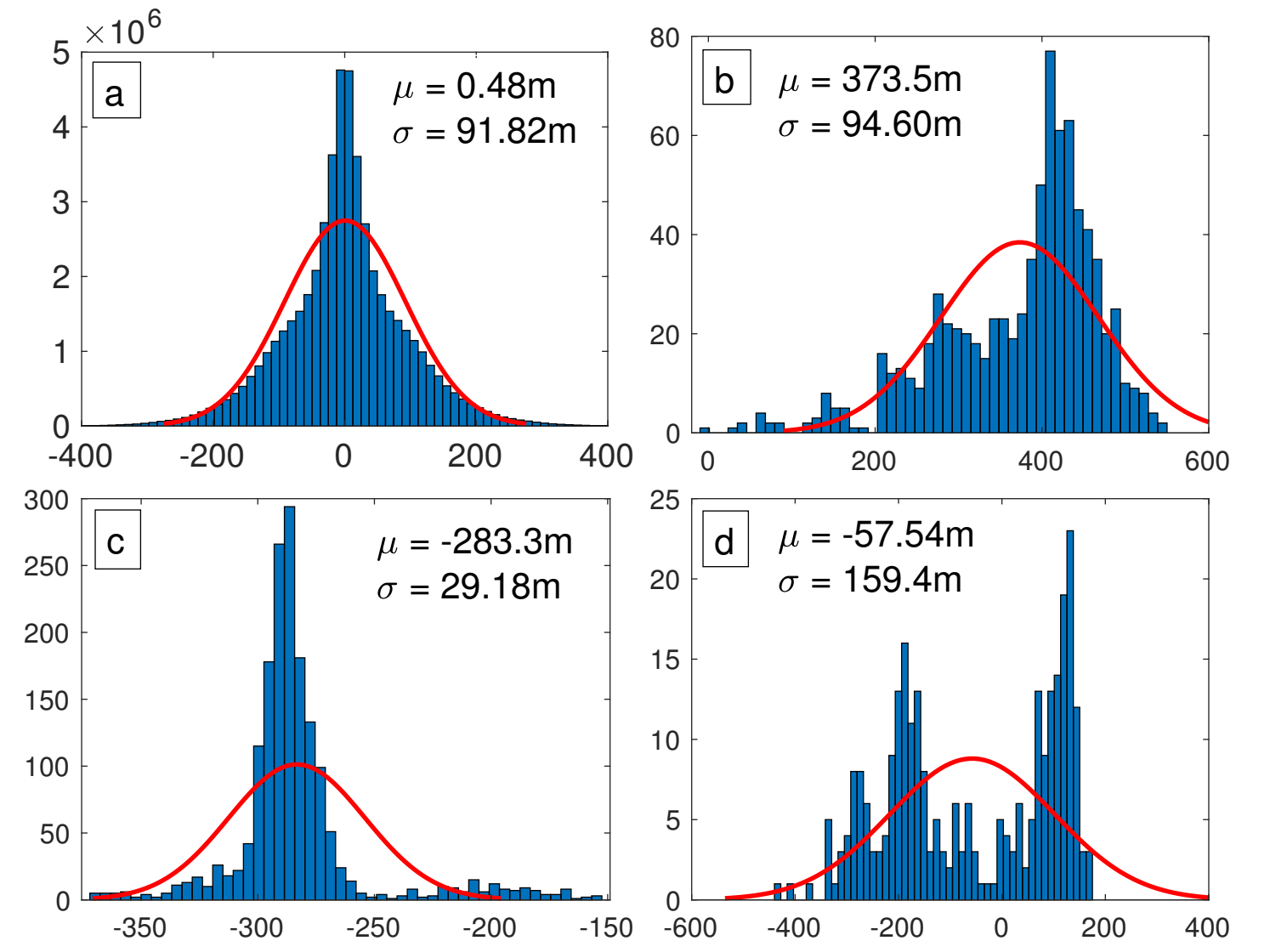
×10^6
a
μ = 0.48m
σ = 91.82m
b
μ = 373.5m
σ = 94.60m
c
μ = -283.3m
σ = 29.18m
d
μ = -57.54m
σ = 159.4m

Figure 4.

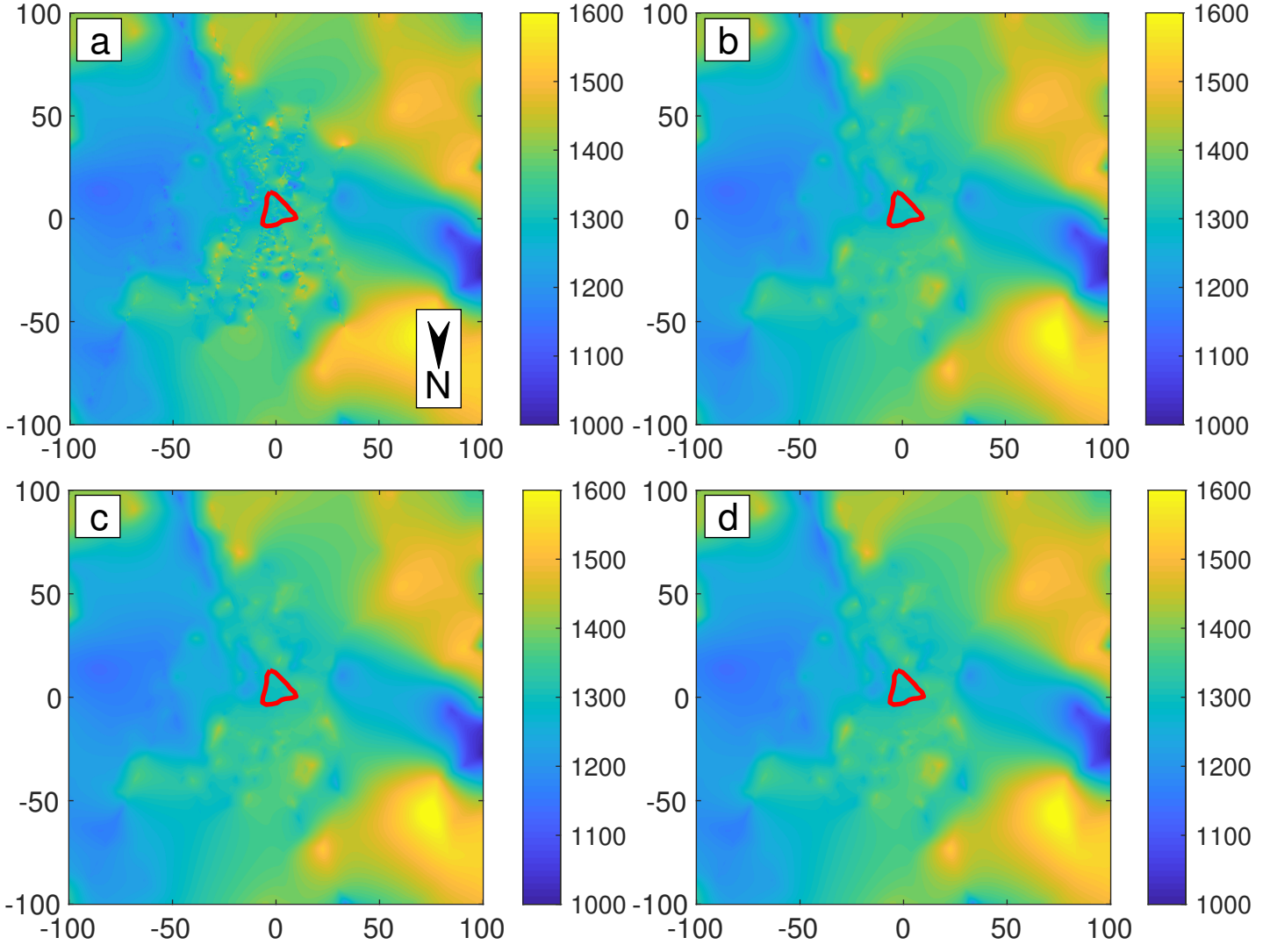
a
b
c
d
N
100
50
0
-50
-100
-100
-50
0
50
100
1600
1500
1400
1300
1200
1100
1000

Figure 5.

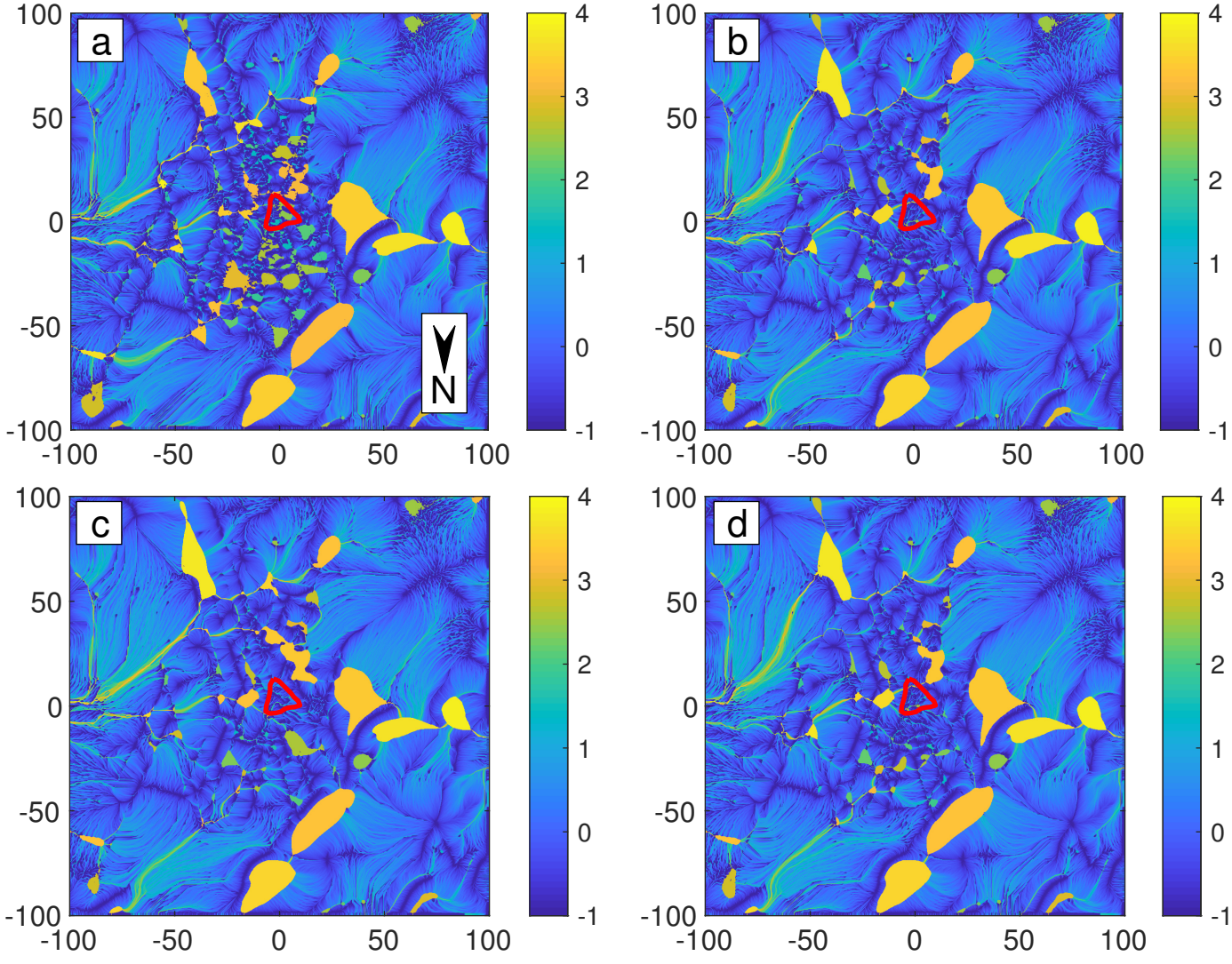
a
b
c
d
N
100
50
0
-50
-100
-100
-50
0
50
100
4
3
2
1
0
-1

Figure 6.

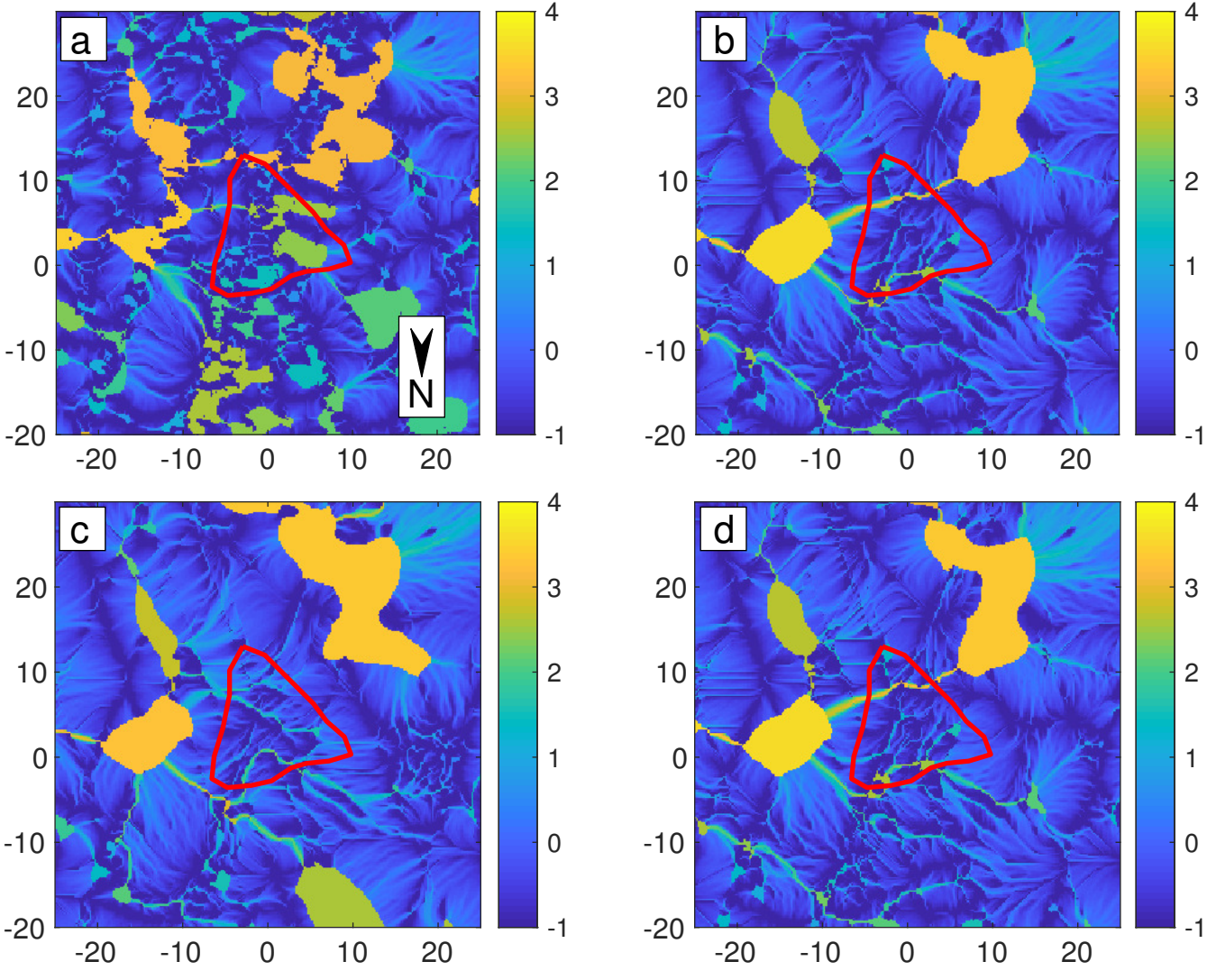
a
b
c
d
N
20
10
0
-10
-20
-20
-10
0
10
20
4
3
2
1
0
-1

Figure 7.

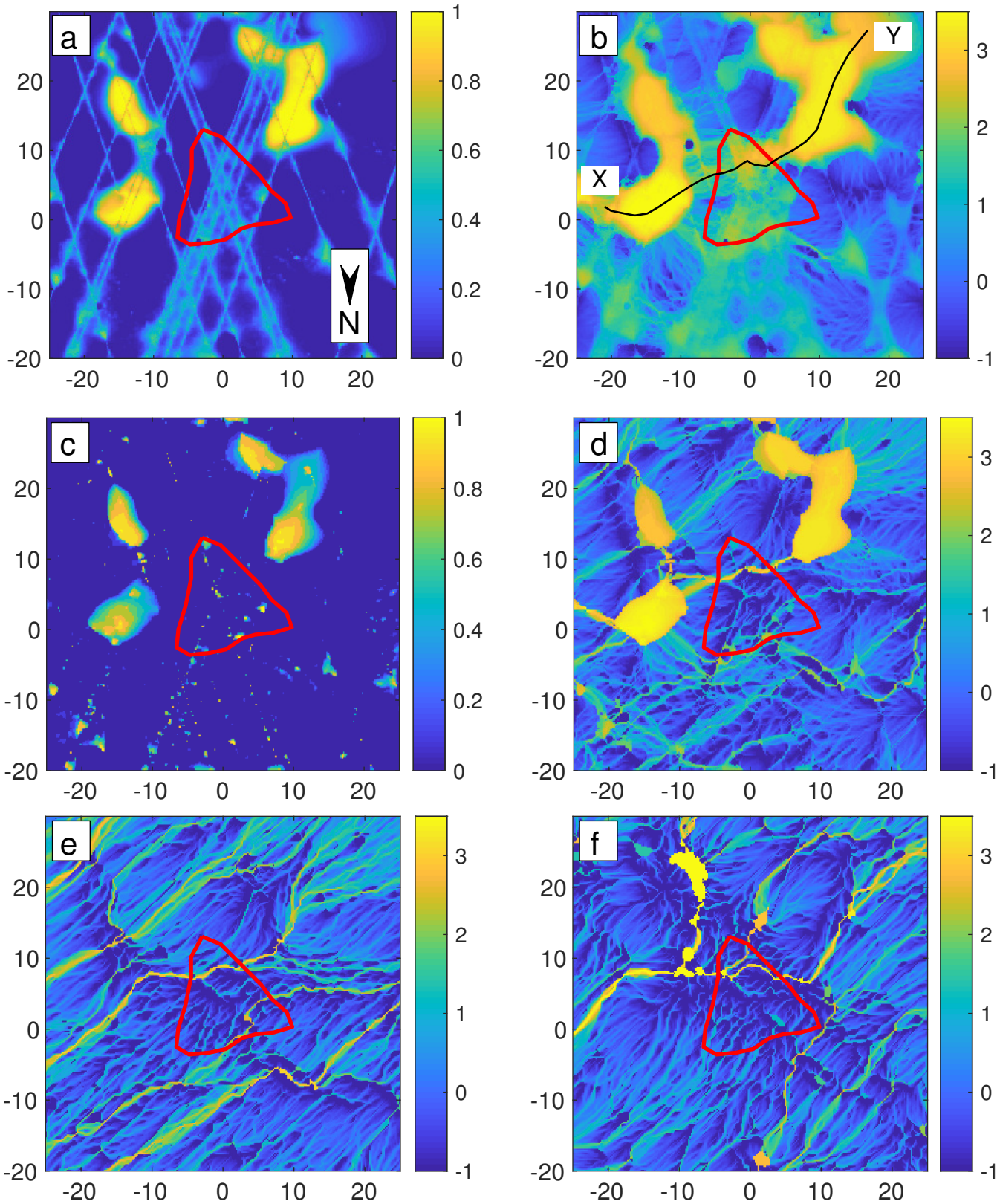
a
N
b
X
Y
c
d
e
f

Figure 8.

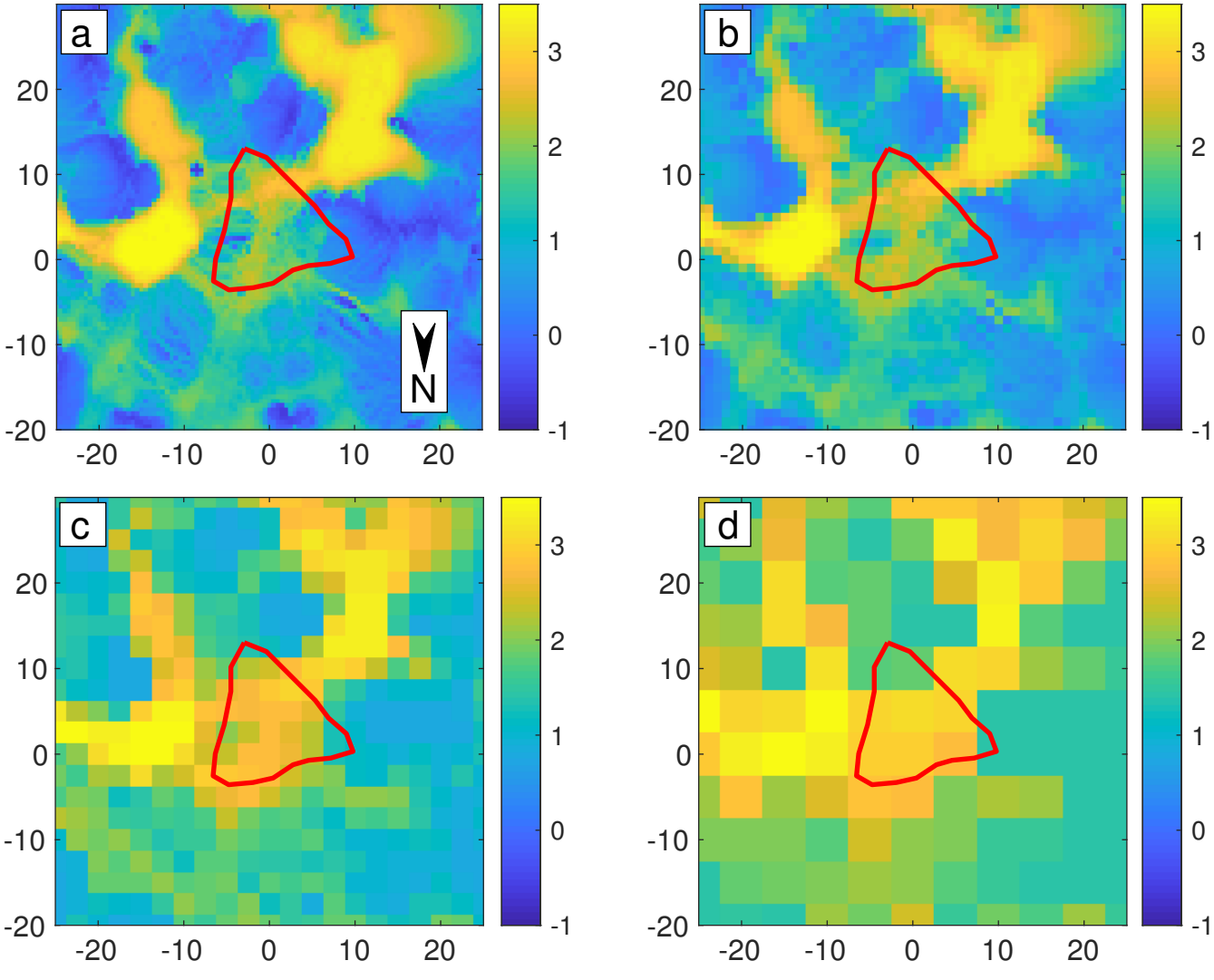
a
b
c
d
N
20
10
0
-10
-20
-20
-10
0
10
20
3
2
1
0
-1

Figure 9.

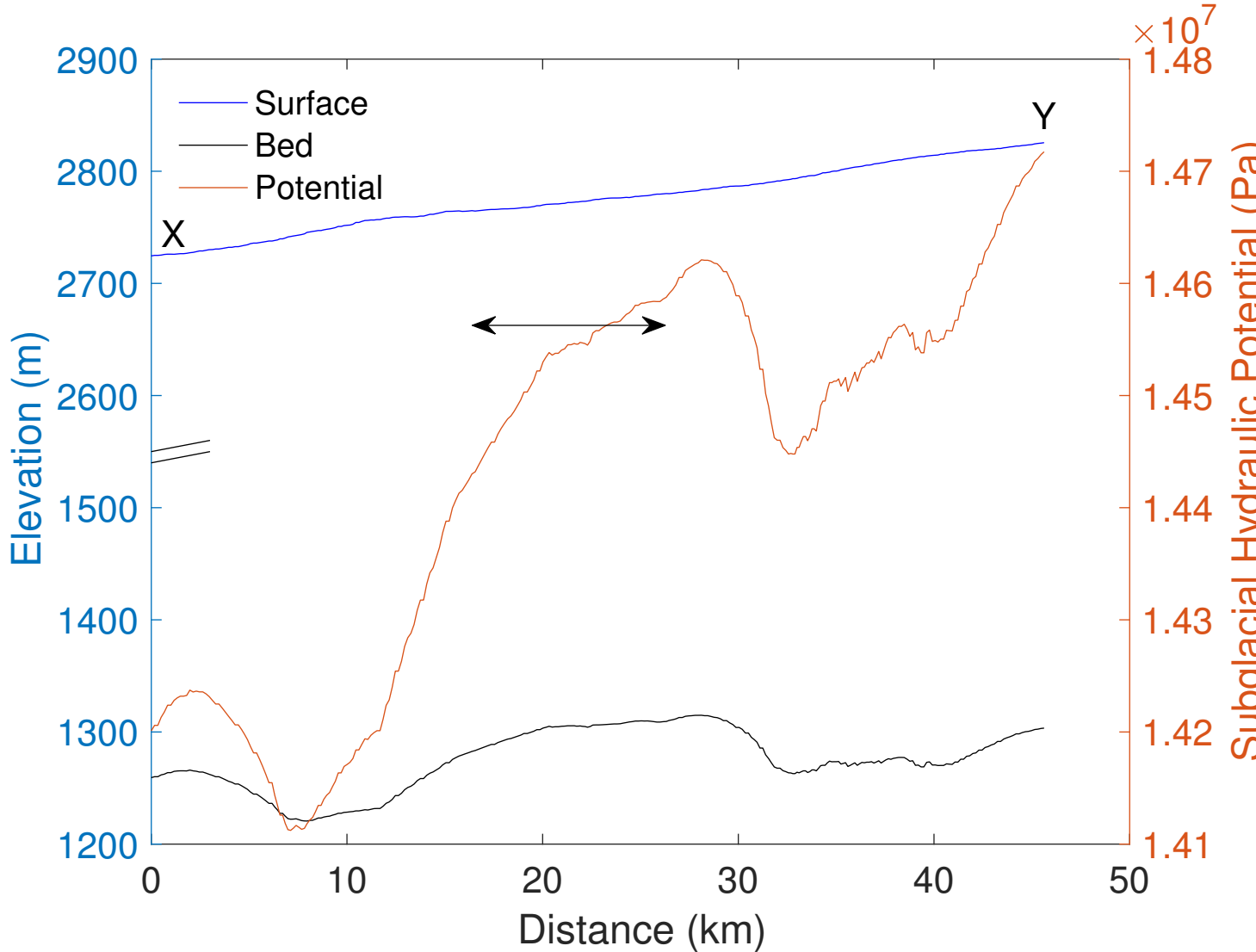
Surface
Bed
Potential
X
Y
2900
2800
2700
2600
1500
1400
1300
1200
Elevation (m)
×10^7
1.48
1.47
1.46
1.45
1.44
1.43
1.42
1.41
Subglacial Hydraulic Potential (Pa)
0
10
20
30
40
50
Distance (km)